Experimental liquid-gas phase transition signals and reaction dynamics

R. Wada,[1] W. Lin (林炜平),[2] P. Ren (任培培),[2] H. Zheng (郑华),[3] X. Liu (刘星泉),[4] M. Huang (黄美容),[5]
K. Yang (杨昆),[6] and K. Hagel[1]

[1]*Cyclotron Institute, Texas A&M University, College Station, Texas 77843, USA*[*]
[2]*Key Laboratory of Radiation Physics and Technology of the Ministry of Education, Institute of Nuclear Science and Technology,
Sichuan University, Chengdu 610064, China*
[3]*School of Physics and Information Technology, Shaanxi Normal University, Xi'an 710119, China*
[4]*Institute of Modern Physics, Chinese Academy of Sciences, Lanzhou 730000, China*
[5]*College of Physics and Electronics Information, Inner Mongolia University for Nationalities, Tongliao 028000, China*
[6]*School of Physics and Engineering Technology, Xingyi Normal University for Nationalities, Xingyi 562400, China*

The experimental liquid-gas phase transition signals are examined for the quasiprojectile (QP) reconstructed from the reactions of ^{40}Ar + ^{27}Al, ^{48}Ti, ^{58}Ni at 47 MeV/nucleon, using measures of caloric curve, multiplicity derivative, moment parameters, and fluctuation of maximum fragment charge number (NVZ). The QP source is reconstructed, using moving source parametrizations on an event-by-event basis. For the determination of the temperature, a quadrupole fluctuation thermometer is used. Deuterons are chosen for the thermometer to minimize the Coulomb and secondary sequential decay effects. A new event-by-event method is proposed for the thermometer to determine the temperature. All measures show a characteristic signature around the temperature $T = 9.0 \pm 0.4$ MeV, which may suggest that the QP system goes into the liquid-gas phase transition at $T_c = 8.3 \pm 0.4$ MeV after the Coulomb correction.

I. INTRODUCTION

In intermediate heavy ion collisions (20 MeV/nucleon $\leqslant E_{\mathrm{inc}} \leqslant$ 300 MeV/nucleon), intermediate mass fragments (IMFs) with $3 \leqslant Z \leqslant 20$ are copiously produced with light particles with $Z \leqslant 2$, which is called a multifragmentation process [1–3]. This multifragmentation process, which was predicted long ago [4], provides a wealth of information on nuclear reaction dynamics and hot nuclear matter studies, especially after the advent of 4π detectors.

Using a variety of the reaction products, a nuclear liquid-gas phase transition was studied as a part of hot nuclear matter studies [5–8]. The nuclear liquid-gas phase transition in the multifragmentation process was first suggested in the early 1980s [9–11]. It is expected to occur when the nucleus is heated to a moderate temperature and breaks up on a short time scale into light particles and IMFs with $Z \geqslant 3$. Based on a statistical equilibrium assumption of the generated hot nuclear matter, different measures have been proposed to probe the liquid-gas phase transition, such as the nuclear specific heat capacity (the caloric curve) [12–20], the negative heat capacity [21,22], the bimodality in charge asymmetry [8,23–25], the Fisher droplet model analysis [26–32], the Landau free energy approach [31–37], the moment of the charge distributions [28,38–41], the fluctuation properties of the heaviest fragment size (charge) [28,29,41–43], the Zipf's law [44,45], the multiplicity derivatives recently proposed by

Mallik *et al.* [46], and the derivative of cluster size [47]. With these features, considerable progress was accomplished on the theoretical side as well as on the experimental side for the nuclear liquid-gas phase transition.

In one of our previous works [48], using events generated by the statistical multifragmentation model (SMM) [49–54], which exhibits a phase transition of the liquid-gas type [55,56], we have demonstrated that most of these measures indeed show a characteristic behavior near or at the phase transition temperature when the extracted measure values are plotted as a function of the temperature. SMM is based on the statistical equilibrium and was somewhat successful in describing the multiple production of IMFs [57–59].

Experimentally, many works have been performed for the reconstructed quasiprojectiles (QPs) and fused systems. In a Multics-Miniball collaboration, QP is reconstructed from peripheral collisions of Au+Au at 35 MeV/nucleon [59] and the occurrence of the negative heat capacity was reported [21,22]. However, Moretto *et al.* cast doubt on the observation [60]. Bimodality was also reported from the INDRA-ALADIN collaboration [24] and the INDRA collaboration [8,61,62] as well as a recent theoretical work of Mallik *et al.* [25]. On the other hand bimodality has also been successfully reproduced by quantum molecular dynamics (QMD) [63–65] and Boltzmann-Uehling-Uhlenbeck (BUU) [66] calculations where memory of the entrance channel is clearly present and thermal equilibrium is not achieved. The signal was interpreted in these studies to have a dynamical origin.

The signatures of different measures for the nuclear liquid-gas phase transition have been experimentally examined in a

[*]wada@comp.tamu.edu

lighter system. Ma *et al.* [28–30] reported that most of the measures mentioned above have been examined as a function of the excitation energy, using the reactions of ^{40}Ar + ^{27}Al, ^{48}Ti, and ^{58}Ni at 47 MeV/nucleon, and reported that all of the examined measures showed a critical behavior around the excitation energy $E^*/A \approx 5.6$ MeV. However, E^*/A increases smoothly around the critical point, and the values of the examined measured quantities do not show a sharp change. On the other hand, if these values are plotted as a function of the temperature, they may show a sharp change at the critical point as observed in SMM simulation [48]. In the above experimental study, only central events were analyzed to ensure that the QP sources are at a fully equilibrated stage. In this article, we revisit the above data set to explore more systematically with a new thermometer to verify the observation of the critical behavior in the previous work [28–30]. In this work all events are examined, including peripheral events, for most of the measures as a function of the temperature on an event-by-event basis to verify the occurrence of the first-order phase transition. To do that, a new method is proposed to evaluate the temperature on an event-by-event basis. This article is organized as follows: A brief description of the experiment and data analysis are given in Sec. II. Temperature determination on an event-by-event basis is described in Sec. III. In Sec. IV, the extracted values of all measures are presented as a function of temperature, assuming all reconstructed QP sources reach a full thermal equilibration. Discussions of the extracted results are made in Sec. V and a summary is given in Sec. VI.

II. EXPERIMENT AND EVENT SELECTION

The reactions of ^{40}Ar + ^{27}Al, ^{48}Ti, ^{58}Ni at 47 MeV/ nucleon have been measured, using the 4π detector, NIMROD (Neutron Ion Multidetector for Reaction Oriented Dynamics) [67], and beams from the TAMU K500 super-conducting cyclotron. Details of the experiments and data analysis have been given in Ref. [28]. The events are sorted according to reaction violence, using the correlation of the associated charged particle multiplicity (M_{CP}) and the neutron multiplicity (M_n). The events are divided into five bins: *Bin* 1 (the most central collisions in the highest multiplicity region of top $\approx$5%), *Bin* 2 (next $\approx$10%), *Bin* 3 (next $\approx$15%), *Bin* 4 (next $\approx$30%), and *Bin* 5 (the most peripheral events, the rest of events). Quasiprojectiles (QPs) are reconstructed and the characteristic nature of the QPs is studied. To reconstruct the QP on an event-by-event basis, moving source (MS) fits have been utilized. Three sources [a quasiprojectile (QP) source, a Nucleon-Nucleon (NN) source, and a quasitarget (QT) source] are used. QP and QT are formulated as a surface emission type of the Maxwellian and a volume emission form is used for NN as described in Ref. [28]. MS fits are performed for all light charged particles (LCPs) and IMFs with $Z \leqslant 5$ for all *Bins* separately. Typical results are shown in Fig. 1. The best χ^2 fits are obtained at $V_s^{PLF} = 8.5 \pm 1.0$ cm/ns and $V_s^{NN} = 5 \pm 1.0$ cm/ns, depending on particle species and the centrality *Bins*. (In this article the χ^2 value is given as that per degree of freedom). The QP selection depends fully on the MS parameters and the choice of three sources is an
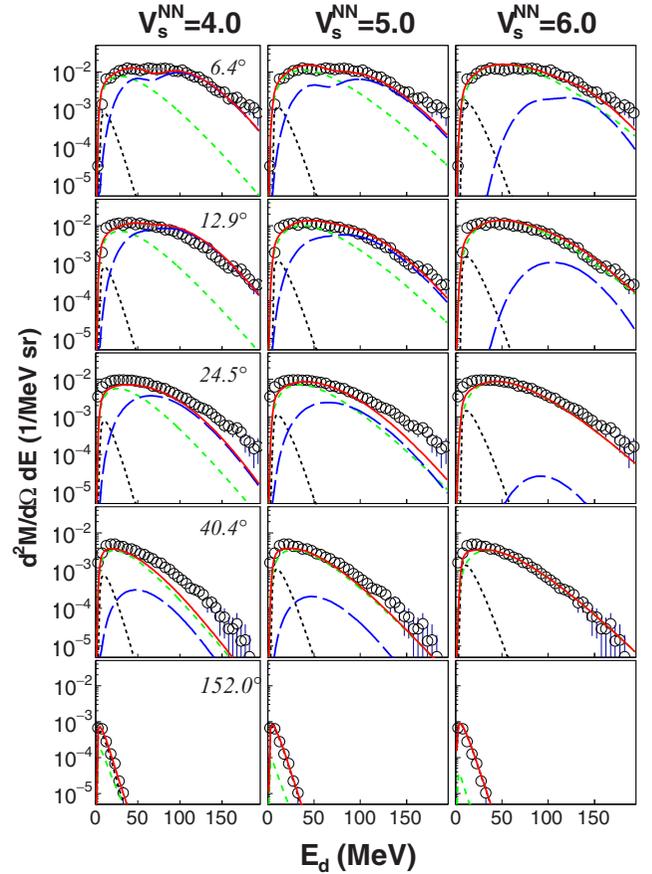
FIG. 1. Moving source fit for deuterons at selected angles for *Bin*1 (most central) of ^{40}Ar + ^{48}Ti at 47 MeV/nucleon. Circles are experimental data and red solid, blue long-dashed, green dashed, and black-dotted curves represent the summed, QP, NN and QT source, respectively. On the left to right column, V_s^{NN} value is set as $V_s^{NN} = 4.0, 5.0, 6.0$ cm/ns. χ^2 values are changed as 2.37, 1.79, 1.64 for $V_s^{NN} = 4.0, 5.0, 6.0$ cm/ns, respectively. The best χ^2 value is 1.63 at $V_s^{NN} = 5.4$ cm/ns.

approximation. To study the dependence of the QP source selection for the following QP analysis, three choices of the MS parameters are provided where the velocity of the NN source is forced to be $V_s^{NN} = 4.0, 5.0,$ and 6.0 cm/ns around its optimum value for all LCPs with $Z \leqslant 2$. For $Z \geqslant 3$, the NN source velocity is treated as a free parameter for all cases.

As shown in Fig. 1 for deuterons, different parameter sets with different V_s^{NN} result in reasonable reproduction of the energy spectra for all particles. This is possible because, when the extracted value of V_s^{NN} is smaller, V_s^{QP} also becomes smaller to include more midrapidity particles and the apparent slope parameter T_{app}^{QP} becomes larger to include the particles in the higher energy side. χ^2 values increase slightly from the best χ^2 value. One should note that there is no clear separation between the QP and NN particles. Similar quality of fits are obtained for all other LCPs except ^{3}He. The ^{3}He fits show significant deviation from the experimental spectrum at $\theta = 64°$ and χ^2 values become slightly worse. However, the multiplicity of ^{3}He is almost 10 times smaller than that of protons and α particles, and therefore the effect on the QP
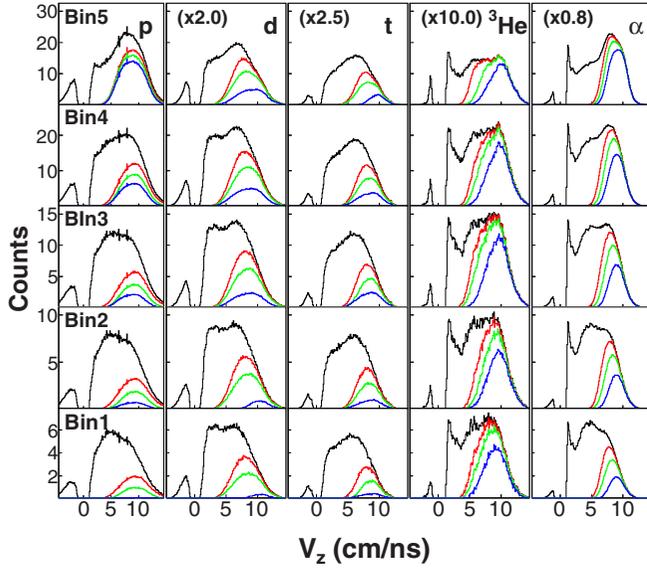
FIG. 2. V_z spectra (z is the beam direction) of $p, d, t,$ ^{3}He, and α particles from left to right for *Bin* 5 (most peripheral) to *Bin* 1 (most central) from top to bottom. Black curves represent the observed experimental spectra and red, green, and blue curves are from the QP particles selected using the MS fit parameters with $V_s^{NN} = 4.0, 5.0,$ and 6.0 cm/ns, respectively. The yields are divided by a factor of 1000, which are also multiplied by the number indicated in the top figure to use the same *Y* axis. 1.0 is used for protons. The same factors are used for different *Bins*.

FIG. 3. QP particle kinetic energy spectra in the QP rest frame for different *Bins* for ^{40}Ar + ^{48}Ti at 47 MeV/nucleon. The QP particles are selected using the MS fit parameters with $V_s^{NN} = 4.0$ cm/ns. Spectra for different *Bins* are shown by different color indicated in the bottom right corner and the particle name is given in each figure.

reconstruction is small. In the actual data analysis, particles belonging to each selection of the QP source, denoted by the V_s^{NN} value hereafter, are determined, using the probability for a certain species of LCP i (i.e., i = p, d, and t, etc.) at a given energy and polar angle θ, $\text{Prob}^{QP}(E_{lab}, \theta, i)$, which is given as

$$\text{Prob}^{QP}(E_{lab}, \theta, i) = \frac{\left(\frac{d^2N}{dE_{lab}d\Omega_{lab}}\right)_i^{QP}}{\left(\frac{d^2N}{dE_{lab}d\Omega_{lab}}\right)_i}. \qquad (1)$$

The denominator, $\left(\frac{d^2N}{dE_{lab}d\Omega_{lab}}\right)_i$, is the yield of particle i for the sum of the three source components and the numerator, $\left(\frac{d^2N}{dE_{lab}d\Omega_{lab}}\right)_i^{QP}$, represents the yield for the QP component.

For a given particle i at an angle θ and a given energy E_{lab} in each event, a random number n is generated and if $n \leqslant \text{Prob}^{QP}(E_{lab}, \theta, i)$, this particle is assigned as a member of the QP source on an event-by-event basis. This procedure also reduces the effect of the slightly poor fits in ^{3}He spectra, because the decision is made by the relative yields between three components. In Fig. 2, typical velocity spectra in the beam direction V_z are shown for the experimental spectra (black) and the QP sources (colored curves) for different *Bins* separately. One should note that all particles in the spectra belong to one of the sources, even though the MS fit does not reproduce the energy spectra for certain species well at certain angles as shown in some of the spectra of Fig. 1 and explained above for the ^{3}He case. When the NN source velocity V_s^{NN} decreases, the contribution of the midrapidity particles to the QP source generally increases. For IMFs with $Z \geqslant 6$, fragments with $V_z/V_Z^{Proj} > 0.65$, are assigned as the

QP component, where V_Z^{Proj} is the projectile velocity. The kinetic energy spectra of particles in the QP rest frame are shown in Fig. 3 for different *Bins* separately. All spectra are well described by a single exponential slope.

To reconstruct the QP source for each case, two corrections are made following Ref. [28]. One is for the missing particles because of the particle detection efficiency of NIMROD. When a QP source is reconstructed, each particle multiplicity of the reconstructed QP is compared to the MS multiplicity of the QP source. If the observed QP multiplicity is lower than the MS value, the difference is counted missing particles and added with randomly generated angle and energy in the QP rest frame, using the MS fit parameters. No correction is made in the rare instances where the observed value is more than the MS value. Another correction is for neutrons. NIMROD provides the associated total neutron multiplicity which is used to determine the event classification. However, it is not possible to divide it into the three source components. In the following analysis, therefore, the associated QP neutron multiplicity is approximated as the difference between the observed neutron number in the reconstructed QP and that of the QP mass A_{QP} with the same N/Z of the projectile, assuming the N/Z of the QP is the same as that of the projectile. The mass number of the observed QP is calculated from the sum of the masses of the detected isotopes and IMFs. The mass of nonisotopically identified IMFs is assumed as $A = 2Z + 1$. The neutron number in the observed QP is also calculated from the sum of the neutrons among isotopes and IMFs. These neutrons are distributed in the QP rest frame using the MS fit parameters of protons, but without Coulomb energy.

In the following QP analysis, only QP events with the experimentally observed QP charge of $12 \leqslant Z_{QP} \leqslant 18$ are used. This minimizes the effect of the corrections, but allows
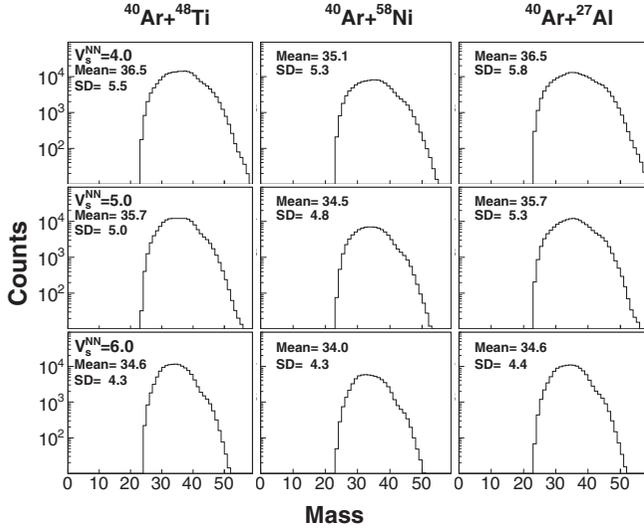
FIG. 4. Reconstructed QP mass distribution of $V_s^{NN} = 4.0$ (top), 5.0 (middle), and 6.0 cm/ns (bottom) for $^{40}\text{Ar} + {}^{48}\text{Ti}$ (left), ^{58}Ni (middle), and ^{27}Al (right). Mean and standard deviation (SD) values of distributions are given in each figure.

FIG. 5. M_{CP} vs E^*/A. Black, red, green, blue, and pink curves are corresponding to *Bin* 1 to *Bin* 5, respectively. Figures are arranged in the same way as Fig. 4.

enough statistics. The lower limit of the charge range from 10 to 14 are also examined, but no significant changes of the results are observed. In Fig. 4, the mass distribution of the reconstructed QP is shown for different QP selections for the three reaction systems studied here. They are very similar for the different QP selections and different target systems. The average QP mass is around 35 ± 1.5.

The excitation energy of the reconstructed QP source is evaluated from the energy balance as

$$E^* = \sum_{i=1}^{M_{CP}} E_i^{\text{kin}}(\text{CP}) + \frac{3}{2} M_n T - Q, \tag{2}$$

where $E_i^{\text{kin}}(\text{CP})$ is the kinetic energy of the charged particle i in the QP rest frame and Q is the reaction Q value. T is taken from the MS fit parameter for the QP source. M_n is the associated QP neutron multiplicity, described above. In Fig. 5, the reconstructed charged particle multiplicity, M_{CP} vs E^*/A, is plotted for the different QP selections for the three reaction systems. For all cases M_{CP} increases as E^*/A increases as expected. However, the rate of increase is slightly slower for *Bin* 5 in most cases and for *Bin* 4 in some cases. We will further discuss this observation in Sec. V. The same behavior was also observed in the previous analyses in Refs. [28–30], and therefore in those analyses only events in *Bin* 1 and 2 were analyzed. Here we take all events.

The contributions of the different centrality events in the QP source are shown in Fig. 6. Events from the two most peripheral collision *Bins* (*Bin* 4 and *Bin* 5) dominate below $E^*/A \leqslant 4 \approx 5$ MeV, indicating that the characteristic features of the QP source for the inclusive data are governed by the events from the two peripheral collision *Bins* below that energy.

III. NUCLEAR THERMOMETER

Different thermometers have been proposed in the past to evaluate the temperature of the hot nuclear matter, such as the slope thermometer [68,69], the isotopic ratio thermometer [70], and the population of excited state thermometer [71,72].

Wuenschel *et al.* [73] proposed a fluctuation thermometer. Using a classical Maxwell-Boltzmann distribution of momentum yields, they derived a temperature from the quadrupole momentum fluctuation of the fragments. The quadrupole
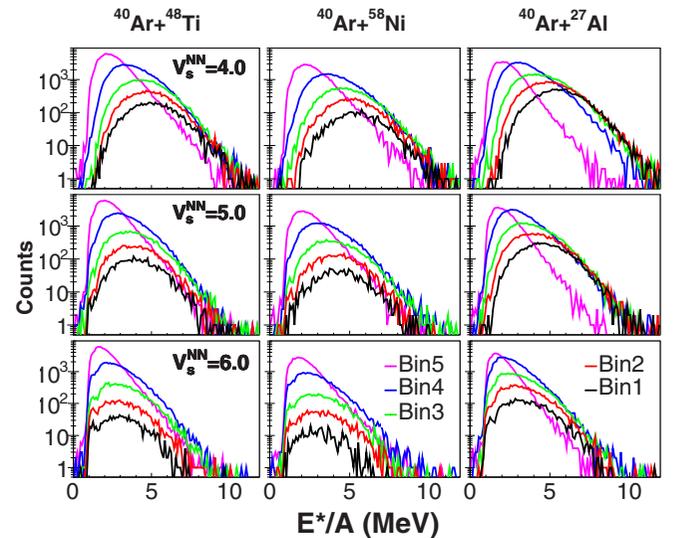
FIG. 6. Excitation energy distributions of different *Bins* for the QP selected with $V_s^{NN} = 4.0, 5.0, 6.0$ cm/ns for $^{40}\text{Ar} + {}^{48}\text{Ti}$, $^{40}\text{Ar} + {}^{58}\text{Ni}$, $^{40}\text{Ar} + {}^{27}\text{Al}$ at 47 MeV/nucleon. *Bin* assignment for different curves is indicated in the figure. Figure arrangement is the same as in Fig. 4.

momentum is defined as

$$Q_{xy} = p_x^2 - p_y^2, \quad (3)$$

where p_x and p_y are the transverse components of the particle momentum. When the energy spectra follow the Maxwell-Boltzmann distribution, so as the actual experimental data which are described by a Maxwell-Boltzmann–type moving source fit [15,68,69,74], the variance of Q_{xy}, σ_{xy}, is related to the temperature T by

$$\langle \sigma_{xy}^2 \rangle = 4m^2T^2, \quad (4)$$

where m is the probe particle mass. The quadrupole momentum fluctuation temperature was applied to examine temperatures of hot nuclear matter [73,75,76]. Because the temperature T is expressed by the average value of the fluctuation of the quadrupole momentum, it cannot be used on an event-by-event basis without approximations. Zheng *et al.* have extended this to a quantum quadrupole thermometer, taking into account the quantum effect explicitly [77]. However, as shown below, the classical quadrupole thermometer gives reasonable temperature values for the SMM simulated events and no significant difference between those of LCPs (some are ferminons and some are bosons) as predicted. We use the classical quadrupole thermometer in this study.

A. Deuteron thermometer

When the quadrupole momentum fluctuation thermometer was applied to experimental data, the extracted temperature values differed significantly for different particles used [73,75,76]. This may be caused by the Coulomb interaction and sequential secondary decay process. To study these effects, events generated with SMM [50,51] are examined.

The quadrupole momentum fluctuation thermometer is applied to the SMM events with the source mass of $A_s = 100$ and $Z_s = 45$. Around 1 million events are generated in the excitation energy range of 1 MeV/nucleon to 15 MeV/nucleon. In Fig. 7, the extracted fluctuation temperature values T_{fl} are plotted as a function of the input excitation energy, E^*/A for $Z = 1$ isotopes. $Z = 1$ isotopes are chosen to minimize the Coulomb effect. In the SMM, the temperature value can be calculated from the energy balance. However, the evaluated temperature for a given event depends slightly on the fragmenting exit channel and therefore depends on different fragments. In the analysis, T_{SMM} is determined as an average value over temperature values of all events at a given excitation energy [54]. These are presented by closed circles. The extracted fluctuation temperature values from the primary fragments before the afterburner, presented by red circles, show very similar behavior for the three isotopes. They are more or less parallel to the T_{SMM} values with some offset energies of about 3 MeV. These higher temperatures may originate from the Coulomb interaction. To verify this, a Coulomb correction is made according to Ref. [78]. The corrected values, presented by green squares, are very close to those of T_{SMM} for protons and deuterons, but are slightly lower for tritons. The thermometer is also applied to the secondary events, using the built-in afterburner in the SMM. For protons, the extracted temperature values, shown by blue triangles,
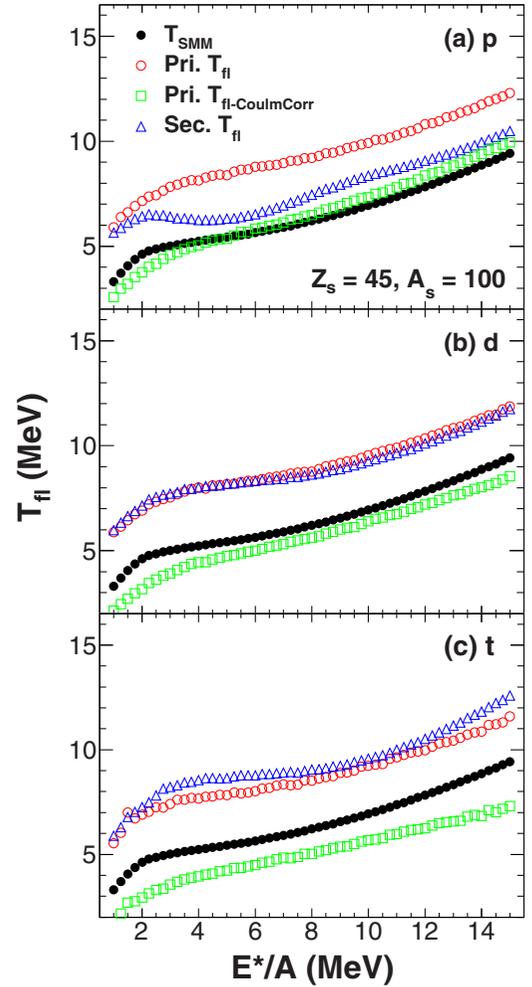
FIG. 7. Quadrupole momentum fluctuation temperatures (T_{fl}) of SMM with $A_s = 100$ and $Z_s = 45$ for (a) protons, (b) deuterons, and (c) tritons. T_{SMM} is the average temperature calculated from the SMM input value. Open circles represent the extracted T_{fl} values from the primary particles and triangles are for those after the secondary decays. Squares represent the Coulomb corrected T_{fl} values of the primary particles.

differ significantly from those of the primary. On the other hand, the extracted temperatures for deuterons are very similar to those of the primary indicating that the secondary decay effect is minimized, and a similar small effect is observed for tritons. This study leads us to select deuterons as the probe of the quadruple momentum fluctuation thermometer in the following analysis.

B. Temperature evaluation on an event-by-event basis

In this article, we propose an additional new method to determine the temperature on an event-by-event basis as follows. In Fig. 8(a), the evaluated T_{fl} values from Eq. (4) with deuterons are plotted by open circles as a function of E^*/A for the ^{40}Ar + ^{48}Ti reaction with the QP selection of $V_s^{NN} = 4.0$ cm/ns.

FIG. 9. T_{fl} vs E^*/A for the different QP selections and the three reactions. T_{fl} is calculated on an event-by-event basis. Figure arrangement is the same as those in Fig. 4. Z scale is the same for all figures and plotted in a logarithmic scale.

Here G(1) is the random number generated according to the Gaussian distribution with $\sigma = 1$ and the average number $< G(1) > = 0$. T_{pol} and ΔT_{pol} values are the calculated values at a given E^*/A, using the polynomial fit parameters extracted beforehand from the average fluctuations. Using this method one can calculate the T_{fl} values on an event-by-event basis and the resultant T_{fl} values are plotted as a function of E^*/A in Fig. 8(c) in which the z axis is given by a logarithmic scale.

IV. RESULTS

The QP events are analyzed, assuming that all ejectiles are emitted at or after the statistical equilibration is achieved. This assumption is supported by the fact that the kinetic energy spectra of all observed particles in the QP rest frame show a single slope as shown in Fig. 3, though the charged particle multiplicity in Fig. 5 shows a slight difference between the central and peripheral events.

Because a wide range of the excitation energy is required for the study, this inclusive procedure enables us to obtain enough statistics at both lower and higher excitation energies in these experimental data sets.

In Fig. 9, the calculated T_{fl} vs E^*/A are shown for the different QP selections and the three reaction systems. A clear plateau is observed starting at around $E^*/A \approx 3$ MeV for the QP selection of $V_s^{NN} = 4.0$ and 5.0 cm/ns in each reaction, but these plateaus become less clear for $V_s^{NN} = 6.0$ cm/ns because of the lower statistics at higher excitation energies. All spectra for $V_s^{NN} = 4.0$ cm/ns show that the temperature increases again at $E^*/A > 6$ MeV. We will discuss further the plateau and the second increase in Sec. V.

A. Specific heat capacity

The specific heat capacity C_V is calculated from the caloric curve as

$$C_V = d(E^*/A)/dT_{fl}. \qquad (6)$$

FIG. 8. Experimental deuteron quadrupole momentum fluctuation temperature T_{fl} in (a) and the standard deviation values ΔT_{fl} in (b), as a function of E^*/A for inclusive data of ^{40}Ar + ^{48}Ti at 47 MeV/nucleon with the QP selection of $V_s^{NN} = 4.0$ cm/ns. Curves in (a) and (b) are from a polynomial fit. (c) Calculated T_{fl} vs E^*/A distribution using the fit parameters in (a) and (b) on the event-by-event basis. Z axis is the yield given by a logarithmic scale.

In Fig. 8(b), the standard deviation values of the T_{fl} are plotted by symbols. The standard deviation values are evaluated, using the TProfile class of ROOT in the CERN data analysis library, which gives the mean and standard deviation values for the calculated values. The fluctuation increases significantly for $E^*/A > 8$ MeV because of statistical errors. These data are fitted by polynomial functions as shown by the solid curves in each figure. One should note that for a given E^*/A value, T_{fl} value is determined within a somewhat small error of ΔT_{fl}, less than 0.5 MeV up to $E^*/A \leqslant 6$ MeV and 1 MeV up to $E^*/A \leqslant 8$ MeV. Based on this observation, the temperature of the reconstructed QP is evaluated on an event-by-event basis, using these polynomial fit parameters, as

$$T_{fl} = T_{pol}(E^*/A) + \Delta T_{pol}(E^*/A) * G(1). \qquad (5)$$

FIG. 10. Specific heat capacity C_V vs T_{fl}. Experimental data are shown by symbols and red curves are a Gaussian fit around the peak. The mean and sigma values of the Gaussian are given in each figure. Figure arrangement is the same as that in Fig. 4.

FIG. 11. Multiplicity derivative dM_{CP}/dT_{fl} vs T_{fl}. Experimental data are shown by symbols and red curves are a Gaussian fit around the peak. The mean and sigma values of the Gaussian are given in each figure. Figure arrangement is same as in Fig. 4.

The calculated C_V values from Fig. 9 are plotted as a function of T_{fl} in Fig. 10. Clear peaks, which correspond to the plateau mentioned above, are observed for $V_s^{NN} = 4.0$ and 5.0 cm/ns. The widths of the peaks are around $1-2$ MeV and increase for $V_s^{NN} = 6.0$ cm/ns where the higher temperature side of the peak is perturbed significantly by lower statistics. The peak values observed in the upper two rows are around 9.0 ± 0.4 MeV. As shown in Fig. 7 the Coulomb correction is not negligible even for $Z=1$ isotopes. The Coulomb correction for a system of $Z = 45/A = 100$ is evaluated to be 3 MeV according to Ref. [78] as shown in the figure. For $A_{QP} = 40$ with $Z_{QP} = 18$, a Coulomb correction of 0.7 MeV is evaluated and therefore the phase transition temperature of $T_c = 8.3 \pm 0.4$ MeV is determined.

B. Multiplicity derivatives

The derivatives of total multiplicity and IMF multiplicity were recently proposed as an observable to search for nuclear liquid-gas phase transition by Mallik *et al.* [46]. We apply this method to the total charged particle multiplicity of the QP sources and results are shown in Fig. 11. The results are very similar to those of C_V in Fig. 10. Similar peaks are observed at similar temperatures with similar widths in each case. This is because, as shown in Fig. 5, E^*/A and M_{CP} are directly related to each other, and therefore $C_V = \frac{d(E^*/A)}{dT}$ and $\frac{dM_{CP}}{dT}$ give the same information for the critical behavior as pointed out in Ref. [46].

C. Normalized variance of Z_{max} (NVZ)

The fluctuation of the order parameter proposed by Botet in Ref. [79] provides a method to select an order parameter, which characterizes critical and off-critical behavior, without an equilibrium assumption. The fluctuation in the atomic

number of the largest fragment (Z_{max}) is one of them and was applied in the analysis of INDRA data in Ref. [80]. The normalized variance of Z_{max} (NVZ) was utilized by Dorso *et al.*, in Ref. [81] to investigate the fluctuation of Z_{max}, which is given as

$$\text{NVZ} = \frac{\sigma_{Z_{max}}^2}{\langle Z_{max} \rangle}. \qquad (7)$$

Here we apply the root-mean-square value of Z_{max} as $\sigma_{Z_{max}}$ in NVZ. Figure 12(a) shows NVZ values as a function of T_{fl} for the $^{40}\text{Ar} + ^{48}\text{Ti}$ reaction with the QP selection of $V_s^{NN} = 4.0$ cm/ns. One can see a peak at 9 MeV over a broad monotonic increasing background. The peak is fitted by a Gaussian distribution. The peak and width values coincide with those of C_V in Fig. 10. These characteristic features are very similar to those of the other reaction systems and the different QP selections, though the peak energies and widths are slightly different as seen in Figs. 10 and 11. The resemblance in the extracted values between the different reaction systems and the different QP selections are also roughly true for the M_2 and γ_2 values discussed in the next subsection. The variation of these parameters are summarized in Sec. IV E.

D. Moment parameters

The general definition of the kth moment [28,38,39] of charge distribution is given as

$$M_k = \sum_{Z_i \neq Z_{max}} n_i(Z_i) Z_i^k, \qquad (8)$$

where $n_i(Z_i)$ is the multiplicity of fragment with charge number $Z = Z_i$ in each event. Using the zeroth (M_0), first (M_1), and second (M_2) moments, the quantity γ_2 is defined as

$$\gamma_2 = \frac{M_2 M_0}{M_1^2}. \qquad (9)$$
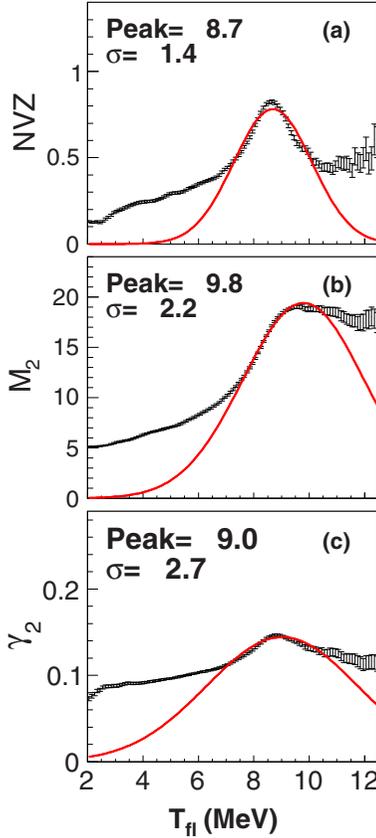
FIG. 12. (a) NVZ, (b) M_2, (c) γ_2 as a function of T_{fl} for the QP selection with $V_s^{NN} = 4.0$ cm/ns of ^{40}Ar + ^{48}Ti at 47 MeV/nucleon. Experimental data are shown by symbols and red curves are a Gaussian fit around the peak. The peak and width values of the Gaussian are given in each figure.

M_2 and γ_2 are expected to show the critical behavior at which the fluctuation of fragment sizes becomes the largest. In Fig. 12(b), M_2 values are plotted. As one can see, M_2 values do not show a peak, but become a maximum at the temperature of ≈ 10 MeV. The distribution shows a plateau after the maximum. The spectrum is fitted by a Gaussian distribution, limiting on the lower temperature side of the maximum. Extracted peak and σ values are shown in the figure and the peak temperature is slightly higher than that of C_V by about 1 MeV, but the temperature of the maximum depends slightly on the width of the Gaussian distribution. In Fig. 12(c), γ_2 values are plotted. One can see a small peak over a large continuous background. A Gaussian fit is made around this small peak and therefore it has a large width. The peak temperature is consistent to those of C_V in Fig. 10 and dM/dT in Fig. 11, even though the peak is small on a large smooth background.

E. Brief summary

In Fig. 13, a summary plot is shown for the extracted peak or maximum values and the widths as a function of T_{fl}. Because the statistics of $V_s^{NN} = 6.0$ cm/ns data is somewhat poor and all the peaks that appear in the measurements are
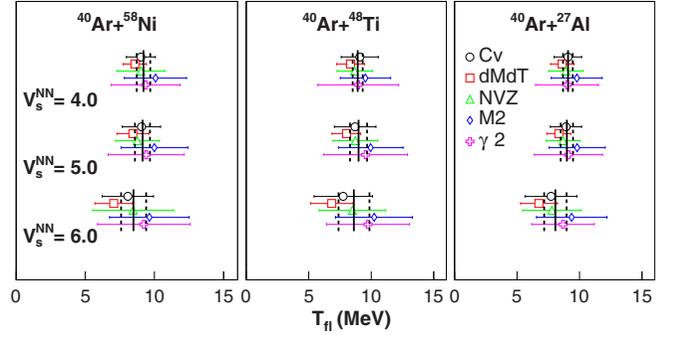
FIG. 13. Summary of the extracted peak or maximum temperatures of all examined measures. Extracted values are plotted from left to right column for ^{40}Ar + ^{58}Ni, ^{40}Ar + ^{48}Ti, ^{40}Ar + ^{27}Al, respectively, and the different QP selections with $V_s^{NN} = 4.0, 5.0, 6.0$ cm/ns from top to bottom. The error bars represent the standard deviation of the peak values.

somewhat broad, the average peak temperature and width are determined from results of $V_s^{NN} = 4.0$ and 5.0 cm/ns and the phase transition temperature $T_c = 8.3 \pm 0.4$ MeV is obtained after the Coulomb correction. One should note that these peak temperatures are very close to the plateau temperature for the system size of $A = 40$–60 in Ref. [82].

V. DISCUSSION

The QP source shows a peak or maximum for all measures examined here at $T_{fl} \approx 9.0 \pm 0.4$ MeV, which is one indication for a first-order phase transition of the QP source with $A_{QP} \approx 35$.

In Fig. 14, the charge distribution of all QP particles Z_{CP} is compared for a given E^*/A value (1 MeV step) and a given *Bin* with that at the same E^*/A value from *Bin* 5, the most peripheral events. Each distribution is normalized to the latter at the α yields. We observe that the shapes in each column are very similar to those of the most peripheral ones (red dashed), especially for *Bin* 4. This resemblance indicates that the distributions are essentially governed by the decay process, but not by the entrance dynamics. At lower excitation energies, the distributions show two peaks, one at $Z_{CP} \approx 15$ and the other at $Z_{CP} = 1$ and 2. This indicates that these events consist mainly of one large fragment and several light particles. This is reminiscent of particle distributions from evaporation decays. At $E^*/A > 2$ MeV, evaporation processes may not be sequential but the decays instead occur simultaneously at the same temperature. However, because the charge distributions resemble those of the evaporation products, we label the process as "evaporation mode" and they are in a liquid state which is represented by the existence of a large IMF. When E^*/A increases beyond 4 MeV, smaller IMFs become dominant. The size of the fragments becomes smaller as E^*/A increases. These IMFs are produced through multi-fragmentation decay and are in a gaslike state, which we label the "multifragmentation mode." $E^*/A = 4$ MeV is a transition energy from the evaporation mode to the multifragmentation mode and this energy region corresponds to the plateau energy in the spectra at $T_{fl} \approx 9$ MeV.
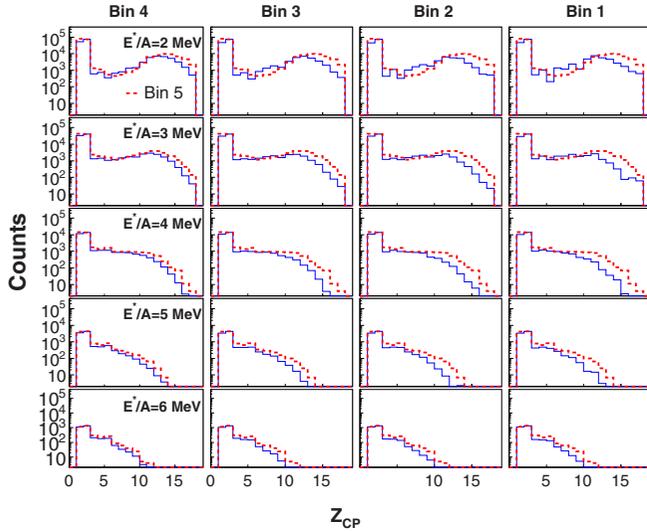
FIG. 14. Charge distribution of QP particles at a given E^*/A for different centrality *Bins*. Plots are arranged for $E^*/A = 2$–6 MeV from the top to the bottom row and *Bins* 4–1 from left to right column. The charge distribution for a given E^*/A and a given *Bin* is shown by a blue solid histogram and that of *Bin* 5 with the same excitation energy is given by a red dashed histogram in each plot for comparison. The blue solid distributions are normalized to the red dashed histograms by the ratio of α yields in each plot.

A clear evolution of the two modes in the charge distribution, an evaporation mode at the lower excitation energies and a multifragmentation mode at the higher excitation energies, shows that the observed plateau in the inclusive data reflects the signature of a liquid-gas phase transition for the QP mass around 35.

One can also notice that the yield of the larger IMFs decreases slightly with increasing centrality at each excitation energy compared to those of *Bin* 5 (red dashed). This reduction may be caused by particle identification inefficiencies of NIMROD. As the centrality increases, larger IMFs have a slightly wider angular distribution where the particle identification is limited for smaller IMFs and becomes increasingly poorer as Z increases beyond 14. This inefficiency may be a possible cause of the nonuniqueness of M_{CP} observed in Fig. 5.

In this study, MS fit parameters are used to assign the QP source on an event-by-event basis. The QP selection is made in three possible midrapidity particle contributions in the QP, using different fixed NN source velocities, V_s^{NN}. The selected QP spectra include all particles on the higher velocity side of the V_z spectra of each particle as shown in Fig. 2 for the different choices of V_s^{NN}. The difference of the QP source for different parameter sets with a given V_s^{NN} comes therefore from the different possible contributions of midrapidity particles, that is, a larger yield of midrapidity particles contribute to the QP source as V_s^{NN} decreases. It should be noted, however, that the reconstructed QP masses are similar after applying missing charged particle and neutron corrections as shown in Fig. 4. When the centrality increases (*Bin* number decreases), the midrapidity particles are enhanced as shown

in Fig. 2 from the top row to the bottom. Therefore different QP selections in this study closely relate to the different centrality selections through the different possible midrapidity particle contributions to the QP source. As shown in Sec. IV, however, no essential difference of the characteristic behavior of the measures was observed between these different QP selections, indicating that the different fraction of midrapidity particle contributions do not affect the extracted fluctuation temperature values.

Another interesting observation in this analysis is a temperature increase after the plateau at $E^*/A > 6$ MeV as shown in Fig. 9. This second increase is observed for all three reactions with $V_s^{NN} = 4.0$ cm/ns. Above $E^*/A = 8$ MeV, as observed in Fig. 8, ΔT_{fl} values become larger than 1 MeV and the width of the T_{fl} distribution increases. However, the centroid of the distributions of T_{fl} in Fig. 9(c) still display a continuous increase. Such a second increase was first reported by Pochodzalla *et al.* in 1995 [17]. In their experiment the Au+Au reaction at 600 MeV/nucleon was performed and analyzed focusing on the forward emitted spectator source. The excitation energy was reconstructed using calorimetry and the temperature was derived from the observed He and Li isotope yield ratio employing the Albergo formalism [70]. In their observation, a significant temperature increase begins at $E^*/A = 10$ MeV after a plateau, suggesting that a vapor phase is revealed in the fragmenting source. However, such a sharp increase was not observed in the EOS collaboration above $E^*/A = 10$ MeV [83]. Therefore the origin of the second increase is still not resolved. Our results suggest that such an increase may begin at $E^*/A = 6$ to 8 MeV, though the trend begins to suffer significantly from poor statistics above $E^*/A = 8$ MeV and we cannot conclude that the observed increase has the same origin as that in Ref. [17]. To confirm the result, further experimental investigation is necessary.

VI. SUMMARY

Phase transition signals predicted by the SMM model simulations in Ref. [48] are examined, using the experimental data of ^{40}Ar + ^{27}Al, ^{48}Ti, ^{58}Ni at 47 MeV/nucleon, taken by the NIMROD 4π detector array. QP source is reconstructed using MS source fits. The MS source fits are made for each particle separately in five centrality *Bins*. Furthermore in each case, three different fixed values of the NN source velocity around the optimum value are applied, which reflect the different amount of contribution from the midrapidity particles in the QP source. A newly proposed fluctuation thermometer of deuteron quadrupole moment is used for the temperature determination on an event-by-event basis. All phase transition related observables examined here show a peak or maximum at $T_c = 8.3 \pm 0.4$ MeV for all cases. This phase transition temperature reflects the transition from the evaporation mode at low temperature to the multifragmentation mode at high temperature. The second increase is also observed at $E^*/A \approx 8$ MeV, but is not well confirmed because of the poor statistics.

[1] K. Hagel, M. Gonin, R. Wada, J. B. Natowitz, F. Haddad, Y. Lou, M. Gui, D. Utley, B. Xiao, J. Li *et al.*, Phys. Rev. C **50**, 2017 (1994).

[2] R. Wada, K. Hagel, J. Cibor, M. Gonin, Th. Keutgen, M. Murray, J. B. Natowitz, A. Ono, J. C. Steckmeyer, A. Kerambrum *et al.*, Phys. Rev. C **62**, 034601 (2000).

[3] R. Wada, T. Keutgen, K. Hagel, Y. G. Ma, J. Wang, M. Murray, L. Qin, P. Smith, J. B. Natowitz, R. Alfarro *et al.*, Phys. Rev. C **69**, 044610 (2004).

[4] N. Bohr, Nature (London) **137**, 344 (1936).

[5] B. Borderie and M. F. Rivet, Prog. Part. Nucl. Phys. **61**, 551 (2008).

[6] F. Gulminelli, W. Trautmann, S. J. Yennello, and P. Chomaz, Eur. Phys. J. A **30**, 1 (2006), and related topics in the volume.

[7] P. Chomaz, M. Colonna, and J. Randrup, Phys. Rep. **389**, 263 (2004).

[8] B. Borderie, E. Bonnet, F. Gulminelli, N. Le Neindre, D. Mercier, S. Piantelli, Ad. R. Raduta, M. F. Rivet, B. Tamain, R. Bougault, A. Chbihi *et al.* (INDRA and ALADIN Collaborations), Nucl. Phys. A **834**, 535c (2010).

[9] J. E. Finn, S. Agarwal, A. Bujak, J. Chuang, L. J. Gutay, A. S. Hirsch, R. W. Minich, N. T. Porile, R. P. Scharenberg, B. C. Stringfellow, and F. Turkot, Phys. Rev. Lett. **49**, 1321 (1982).

[10] R. W. Minich, S. Agarwal, A. Bujak, J. Chuang, J. E. Finn, L. J. Gutay, A. S. Hirsch, N. T. Porile, R. P. Scharenberg, B. C. Stringfellow *et al.*, Phys. Lett. B **118**, 458 (1982).

[11] A. S. Hirsch, A. Bujak, J. E. Finn, L. J. Gutay, R. W. Minich, N. T. Porile, R. P. Scharenberg, B. C. Stringfellow *et al.*, Nucl. Phys. A **418**, 267 (1984).

[12] E. Suraud, C. Grégoire, and B. Tamain, Prog. Part. Nucl. Phys. **23**, 357 (1989).

[13] D. H. E. Gross, Prog. Part. Nucl. Phys. **30**, 155 (1993).

[14] K. Hagel, D. Fabris, P. Gonthier, H. Ho, Y. Lou, Z. Majka, G. Mouchty, M. N. Namboodiri, J. B. Natowitz, G. Nebbia *et al.*, Nucl. Phys. A **486**, 429 (1988).

[15] R. Wada, D. Fabris, K. Hagel, G. Nebbia, Y. Lou, M. Gonin, J. B. Natowitz, R. Billerey, B. Cheynis, A. Demeyer *et al.*, Phys. Rev. C **39**, 497 (1989).

[16] D. Cussol, G. Bizard, R. Brou, D. Durand, M. Louvel, J. P. Patry, J. Péter, R. Regimbart, J. C. Steckmeyer, J. P. Sullivan, B. Tamain, E. Crema, H. Doubre *et al.*, Nucl. Phys. A **561**, 298 (1993).

[17] J. Pochodzalla, T. Möhlenkamp, T. Rubehn A. Schüttauf, A. Wörner, E. Zude, M. Begemann-Blaich, Th. Blaich, H. Emling, A. Ferrero *et al.*, Phys. Rev. Lett. **75**, 1040 (1995).

[18] R. Wada, R. Tezkratt, K. Hagel, F. Haddad, A. Kolomiets, Y. Lou, J. Li, M. Shimooka, S. Shlomo, D. Utley, B. Xiao, N. Mdeiwayeh, J. B. Natowitz, Z. Majka *et al.*, Phys. Rev. C **55**, 227 (1997).

[19] K. Hagel, R. Wada, J. Cibor, M. Lunardon, N. Marie, R. Alfaro, W. Shen, B. Xiao, Y. Zhao, Z. Majka *et al.*, Phys. Rev. C **62**, 034607 (2000).

[20] T. Furuta and A. Ono, Phys. Rev. C **74**, 014612 (2006).

[21] M. D'Agostino, F. Gulminelli, Ph. Chomaz, M. Bruno, F. Cannata, R. Bougault, F. Gramegna, I. Iori, N. Le Neindre, G. V. Margagliotti *et al.*, Phys. Lett. B **473**, 219 (2000).

[22] M. D'Agostino, R. Bougault, F. Gulminelli, M. Bruno, F. Cannata, Ph. Chomaz, F. Gramegna, I. Iori, N. Le Neindre, G. V. Margagliotti *et al.*, Nucl. Phys. A **699**, 795 (2002).

[23] O. Lopez, D. Lacroix, and E. Vient, Phys. Rev. Lett. **95**, 242701 (2005).

[24] M. Pichon, B. Tamain, R. Bougault, F. Gulminelli, O. Lopez, E. Bonnet, B. Borderie, A. Chbihi, R. Dayras, J. D. Frankland *et al.* (INDRA and ALADIN Collaborations), Nucl. Phys. A **779**, 267 (2006).

[25] S. Mallik, G. Chaudhuri, and F. Gulminelli, Phys. Rev. C **97**, 024606 (2018).

[26] M. E. Fisher, Rep. Prog. Phys. **30**, 615 (1969); **3**, 255 (1967).

[27] J. B. Elliott, L. G. Moretto, L. Phair, G. J. Wozniak, L. Beaulieu, H. Breuer, R. G. Korteling, K. Kwiatkowski, T. Lefort, L. Pienkowski, A. Ruangma *et al.*, Phys. Rev. Lett. **88**, 042701 (2002).

[28] Y. G. Ma, J. B. Natowitz, R. Wada, K. Hagel, J. Wang, T. Keutgen, Z. Majka, M. Murray, L. Qin, P. Smith *et al.*, Phys. Rev. C **71**, 054606 (2005).

[29] Y. G. Ma, J. B. Natowitz, R. Wada, K. Hagel, J. Wang, T. Keutgen, Z. Majka, M. Murray, L. Qin, P. Smith *et al.*, Nucl. Phys. A **749**, 106c (2005).

[30] Y. G. Ma, R. Wada, K. Hagel, J. Wang, T. Keutgen, Z. Majka, M. Murray, L. Qin, P. Smith, J. B. Natowitz *et al.*, Phys. Rev. C **69**, 031604(R) (2004).

[31] M. Huang, R. Wada, Z. Chen, T. Keutgen, S. Kowalski, K. Hagel, M. Barbui, A. Bonasera, C. Bottosso, T. Materna *et al.*, Phys. Rev. C **82**, 054602 (2010).

[32] G. Giuliani, H. Zheng, and A. Bonasera, Prog. Part. Nucl. Phys. **76**, 116 (2014).

[33] A. Bonasera, Z. Chen, R. Wada, K. Hagel, J. Natowitz, P. Sahu, L. Qin, S. Kowalski, Th. Keutgen, T. Materna, and T. Nakagawa, Phys. Rev. Lett. **101**, 122702 (2008).

[34] R. Tripathi, A. Bonasera, S. Wuenschel, L. W. May, Z. Kohley, G. A. Souliotis, S. Galanopoulos, K. Hagel, D. V. Shetty, K. Huseman *et al.*, Phys. Rev. C **83**, 054609 (2011).

[35] R. Tripathi, A. Bonasera, S. Wuenschel, L. W. May, Z. Kohley, G. A. Souliotis, S. Galanopoulos, K. Hagel, D. V. Shetty, K. Huseman, S. N. Soisson *et al.*, J. Phys. Conf. Ser. **312**, 082043 (2011).

[36] R. Tripathi, A. Bonasera, S. Wuenschel, L. W. May, Z. Kohley, P. Martini, A. McIntosh, G. A. Souliotis, S. Ganopoulos, K. Hagel, D. V. Shetty *et al.*, Int. J. Mod. Phys. E **21**, 1250019 (2012).

[37] J. Mabiala, A. Bonasera, H. Zheng, A. B. McIntosh, L. W. May, P. Cammarata, Z. Kohley, K. Hagel, L. Heilborn, A. Raphelt *et al.*, Phys. Rev. C **87**, 017603 (2013).

[38] X. Campi, Phys. Lett. B **208**, 351 (1988).

[39] X. Campi, J. Phys. A **19**, L917 (1986).

[40] S. Das Gupta and A. Z. Mekjian, Phys. Rev. C **57**, 1361 (1998).

[41] P. F. Mastinu, M. Belkacem, F. Gramegna, and P. M. Milazzo, Phys. Rev. C **57**, 831 (1998).

[42] R. Botet, M. Płoszajczak, A. Chbihi, B. Borderie, D. Durand, and J. Frankland, Phys. Rev. Lett. **86**, 3514 (2001).

[43] J. D. Frankland, A. Chbihi, A. Mignon, M. L. Begemann-Blaich, R. Bittiger, B. Borderie, R. Bougault, J.-L. Charvet, D. Cussol, R. Dayras *et al.* (INDRA and ALADIN Collaborations), Phys. Rev. C **71**, 034607 (2005).

[44] Y. G. Ma, Phys. Rev. Lett. **83**, 3617 (1999).

[45] Y. G. Ma, Eur. Phys. J. A **6**, 367 (1999).

[46] S. Mallik, G. Chaudhuri, P. Das, and S. Das Gupta, Phys. Rev. C **95**, 061601(R) (2017).

[47] P. Das, S. Mallik, and G. Chaudhuri, Phys. Lett. B **763**, 364 (2018).

[48] W. Lin, P. Ren, H. Zheng, X. Liu, M. Huang, R. Wada, and G. Qu, Phys. Rev. C **97**, 054615 (2018).

[49] X. Z. Zhang, D. H. E. Gross, S. Y. Xu, and Y. M. Zheng, Nucl. Phys. A **461**, 641 (1987).

[50] J. P. Bondorf, A. S. Botvina, A. S. Iljinov, I. N. Mishustin, and K. Sneppen, Phys. Rep. **257**, 133 (1995).

[51] A. S. Botvina and I. N. Mishustin, Phys. Rev. C **63**, 061601(R) (2001).

[52] X. Z. Zhang, D. H. E. Gross, S. Y. Xu, and Y. M. Zheng, Nucl. Phys. A **461**, 668 (1987).

[53] G. A. Souliotis, A. S. Botvina, D. V. Shetty, A. L. Keksis, M. Jandel, M. Veselsky, and S. J. Yennello, Phys. Rev. C **75**, 011601(R) (2007).

[54] W. Lin, H. Zheng, P. Ren, X. Liu, M. Huang, R. Wada, Z. Chen, J. Wang, G. Q. Xiao, and G. Qu, Phys. Rev. C **97**, 044603 (2018).

[55] N. Buyukcizmeci, R. Ogul, and A. S. Botvina, Eur. Phys. J. A **25**, 57 (2005).

[56] R. Ogul, N. Buyukcizmeci, and A. S. Botvina, Nucl. Phys. A **749**, 126c (2005).

[57] A. S. Botvina, I. N. Mishustin, M. Begemann-Blaich, J. Hubele, G. Imme, I. Iori, R Kreutz, G. J. Kunde, W. D. Kunze, V. Lindenstruth *et al.*, Nucl. Phys. A **584**, 737 (1995).

[58] M. D'Agostino, A. S. Botvina, P. M. Milazzo, M. Bruno, G. J. Kunde, D. R. Bowman, L. Celano, N. Colonna, J. D. Dinius, and A. Ferrero *et al.*, Phys. Lett. B **371**, 175 (1996).

[59] M. D'Agostino, A. S. Botvina, M. Bruno, A. Bonasera, J. P. Bondorf, R. Bougault, E. Désesquelles, E. Geraci, F. Gulminelli, I. Iori *et al.*, Nucl. Phys. A **650**, 329 (1999).

[60] L. G. Moretto, J. B. Elliott, L. Phair, and G. J. Wozniak, Phys. Rev. C **66**, 041601R (2002).

[61] B. Boadrie, S. Piantelli, M. F. Rivet, Ad. R. Raduta, G. Ademard, E. Bonnet, R. Bougault, A. Chbihi, J. D. Frankland, E. Galichet *et al.*, Phys. Lett. B **723**, 140 (2013).

[62] M. D'Agostino, M. Bruno, F. Gulminelli, F. Cannata, Ph. Chomaz, G. Casini, E. Geraci, F. Gramegna, A. Moroni, G. Vannini *et al.*, Nucl. Phys. A **749**, 55 (2005).

[63] K. Zbiri, A. Le Fèvre, J. Aichelin, J. Lukasik, W. Reisdorf, F. Gulminelli, U. Lynen, W. F. J. Müller, H. Orth, C. Schwarz *et al.*, Phys. Rev. C **75**, 034612 (2007).

[64] A. Le Fèvre and J. Aichelin, Phys. Rev. Lett. **100**, 042701 (2008);

[65] A. Le Fèvre, J. Aichelin, C. Hartnack, J. Łukasik, W. F. J. Müller, H. Orth, C. Schwarz, C. Sfienti, W. Trautmann, K. Turzó *et al.*, Phys. Rev. C **80**, 044615 (2009).

[66] S. Mallik, S. Das Gupta, and G. Chaudhuri, Phys. Rev. C **93**, 041603 (2016).

[67] S. Wuenschel, K. Hagel, R. Wada, J. B. Natowitz, S. J. Yennello, Z. Kohley, C. Bottosso, L. W. May, W. B. Smith, D. V. Shetty *et al.*, Nucl. Inst. Meth. A **604**, 578 (2009).

[68] G. D. Westfall, B. V. Jacak, N. Anantaraman, M. W. Curtin, G. M. Crawley, C. K. Gelbke, B. Hasselquist, W. G. Lynch, D. K. Scott, B. M. Tsang *et al.*, Phys. Lett. B **116**, 118 (1982).

[69] B. V. Jacak, G. D. Westfall, C. K. Gelbke, L. H. Harwood, W. G. Lynch, D. K. Scott, H. Stocker, M. B. Tsang, and T. J. M. Symons, Phys. Rev. Lett. **51**, 1846 (1983).

[70] S. Albergo, S. Costa, E. Costanzo, and A. Rubbino, Nuovo Cimento A **89**, 1 (1985).

[71] D. J. Morrissey, W. Benenson, E. Kashy, B. Sherrill, A. D. Panagiotou, R. A. Blue, R. M. Ronningen, J. van der Plicht, and H. Utsunomiya, Phys. Lett. B **148**, 423 (1984).

[72] J. Pochodzalla, W. A. Friedman, C. K. Gelbke, W. G. Lynch, M. Maier, D. Ardouin, H. Delagrange, H. Doubre, C. Grégoire, A. Kyanowski *et al.*, Phys. Rev. Lett. **55**, 177 (1985).

[73] S. Wuenschel, A. Bonasera, L. W. May, G. A. Souliotis, R. Tripathi, S. Galanopoulos, Z. Kohley, K. Hagel, D. V. Shetty, K. Huseman *et al.*, Nucl. Phys. A **843**, 1 (2010).

[74] T. C. Awes, S. Saini, G. Poggi, C. K. Gelbke, D. Cha, R. Legrain, and G. D. Westfall, Phys. Rev. C **25**, 2361 (1982).

[75] A. B. McIntosh, A. Bonasera, P. Cammarata, K. Hagel, L. Heilborn, Z. Kohley, J. Mabiala, L. W. May, P. Marini, A. Raphelt, G. A. Souliotis *et al.*, Phys. Lett. B **719**, 337 (2013).

[76] A. B. McIntosh, A. Bonasera, Z. Kohley, P. J. Cammarata, K. Hagel, L. Heilborn, J. Mabiala, L. W. May, P. Marini, A. Raphelt, G. A. Souliotis *et al.*, Phys. Rev. C **87**, 034617 (2013).

[77] H. Zheng and A. Bonasera, Phys. Lett. B **696**, 178 (2011).

[78] H. Zheng, G. Giuliani, and A. Bonasera, J. Phys. G: Nucl. Part. Phys. **41**, 055109 (2014).

[79] R. Botet and M. Płoszajczak, Phys. Rev. E **62**, 1825 (2000).

[80] B. Borderie, J. Phys. G : Nucl. Part. Phys. **28**, R217 (2002).

[81] C. O. Dorso, V. C. Latora, and A. Bonasera, Phys. Rev. C **60**, 034606 (1999).

[82] J. B. Natowitz, R. Wada, K. Hagel, T. Keutgen, M. Murray, A. Makeev, L. Qin, P. Smith, and C. Hamilton, Phys. Rev. C **65**, 034618 (2002).

[83] J. A. Hauger, P. Warren, S. Albergo, F. Bieser, F. P. Brady, Z. Caccia, D. A. Cebra, A. D. Chacon, J. L. Chance, Y. Choi *et al.*, Phys. Rev. C **57**, 764 (1998).